Solid State Ionics 429 (2025) 116962

Contents lists available at ScienceDirect

Solid State Ionics

journal homepage: www.elsevier.com/locate/ssi

Thermodynamics, local structure, and transport of protons in triple-conducing oxide, $BaCo_{0.4}Fe_{0.4}Zr_{0.1}Y_{0.1}O_{3-\delta}$ (BCFZY4411)☆

Yewon Shin [a,*], Michael D. Sanders [a], Erica Truong [b], Supriyo Majumder [c], Bernadette Cladek [d], Michael Walker [a], Bright Ogbolu [b], Rongfu Zhang [b], Guennadi A. Evmenenko [c], Yan-Yan Hu [b,f], Michael J. Bedzyk [c,g], Katharine Page [d,e], Sossina M. Haile [c], Ryan O'Hayre [a]

[a] Department of Metallurgical and Materials Engineering, Colorado School of Mines, Golden, CO 80401, USA
[b] Department of Chemistry, Florida State University, Tallahassee, FL 32310, USA
[c] Department of Materials Science and Engineering, Northwestern University, Evanston, IL 60208, USA
[d] Department of Materials Science and Engineering, University of Tennessee-Knoxville, Knoxville, TN 37996, USA
[e] Neutron Scattering Division, Oak Ridge National Laboratory, Oak Ridge, TN 37831, USA
[f] Center of Interdisciplinary Magnetic resonance, National High Magnetic Field Laboratory, Tallahassee, FL 32310, USA
[g] Department of Physics and Astronomy, Northwestern University, Evanston, IL 60208, USA

ARTICLE INFO

Keywords:
Triple-conducting oxide (TCO)
Positrode
BCFZY4411
Kinetics
Thermodynamics
Local structure and dynamics

ABSTRACT

Triple-conducting oxides (TCOs) are an emerging class of mixed ionic and electronically conducting materials that show great promise for oxygen reduction/evolution (ORR/OER) electrocatalysis—primarily in high-temperature ceramic electrochemical cells— but also in aqueous alkaline environments. Their high activity is attributed, at least in part, to their ability to incorporate and transport three mobile charge carriers: protons, oxygen vacancies, and electron-holes. Despite their promise, fundamental studies of TCOs are challenging, as transport dynamics from three charge carriers cannot be fully disentangled via traditional electrical measurement techniques. Characterizing proton dynamics in TCOs is particularly difficult as protons are generally the minority carrier, and their conduction response is typically obscured by the oxygen vacancies and electron holes. Here, we demonstrate successful isolation of the proton behavior in an archetypal TCO, $BaCo_{0.4}Fe_{0.4}Zr_{0.1}Y_{0.1}O_{3-\delta}$ (BCFZY4411), using a combination of non-electrical techniques. We determine proton uptake and oxygen non-stoichiometry (δ) using thermogravimetric analysis (TGA). X-ray absorption near edge structure (XANES) and neutron diffraction (ND) are used to validate the oxidation state of Co and the δ values obtained through TGA. We apply ^{1}H solid-state magic-angle-spinning (MAS) nuclear magnetic resonance (NMR) to provide insights into local structure, dynamics, and proton kinetics. Finally, the proton transport properties are further quantified using tracer isotope exchange with time-of-flight secondary ion mass spectrometry (ToF-SIMS). Despite the very low proton concentrations in BCFZY4411 (<0.2 % under most conditions), our analysis suggests that the oxygen reduction and evolution reactions are nevertheless limited by the oxygen ion kinetics (e.g., oxygen surface exchange) rather than the proton kinetics at the reduced operating temperatures (<500 °C) that are targeted for electrochemical cell applications. These findings provide a comprehensive understanding of proton behavior in BCFZY4411 and pave the way for advancing the fundamental study of TCOs.

1. Introduction

Triple-conducting oxides (TCOs) are a unique subset of mixed ion-electron conducting (MIEC) materials that facilitate the transport of three distinct charge carriers, typically protons ($OH_O^{\bullet}$), oxygen vacancies ($V_O^{\bullet\bullet}$), and electron holes ($h^{\bullet}$). This mixed transport behavior contributes significantly to their promising electrocatalytic activity, particularly for the oxygen reduction and oxygen evolution reactions (ORR/OER) in fuel cells and electrolyzers, as these reactions can potentially involve all three defect species as key reaction intermediates. TCOs have enabled record-breaking performance in both protonic ceramic electrochemical cells (PCCs) as well as conventional oxygen ion-conducting solid oxide

☆ This article is part of a Special issue entitled: 'Solid State Ionics 100' published in Solid State Ionics.

* Corresponding author.
E-mail address: shin@mines.edu (Y. Shin).

https://doi.org/10.1016/j.ssi.2025.116962
Received 11 April 2025; Received in revised form 17 June 2025; Accepted 5 July 2025
Available online 11 July 2025

electrochemical cells (SOCs) [1], e.g., for high-temperature fuel cell and electrolysis applications. They have also demonstrated promising performance in low-temperature alkaline cells [2].

$BaCo_{0.4}Fe_{0.4}Zr_{0.1}Y_{0.1}O_{3-\delta}$ (BCFZY4411) is a prototypical and widely used TCO [1,3–5]. The low electronegativity (χ) of Ba ($\chi = 0.89$) enhances oxygen-site basicity and proton uptake, while Y doping generates oxygen vacancies crucial for ionic conduction (H^+ and O^{2-}). Multivalent transition metals (TMs), Co and Fe, facilitate electronic conduction via mobile polaronic electron-holes hopping along TM-O-TM bonds, while their redox flexibility supports catalytic activity for the relevant electrochemical reactions (ORR/OER). Given these attributes, BCFZY4411 has been highly effective, demonstrating exceptional performance in both PCCs and SOCs [6–11].

Fundamental studies of BCFZY4411 have primarily focused on oxygen vacancy [12–14] and/or proton transport [15–18], motivated by the desire to enhance their performance in electrochemical cells as positrodes. These studies have typically employed electrical conductivity relaxation (ECR), yielding kinetic properties that result from changes in the coupled chemical potential gradients of the charge carriers. This complicates the interpretation of the transport physics and obscures a clear understanding of the kinetic behavior of each charge carrier. To isolate individual charge carrier contributions, Shin et al. utilized the isotope exchange technique, in particular to study oxygen ion kinetics in various $BaCo_xFe_{0.8-x}Zr_{0.1}Y_{0.1}O_{3-\delta}$ (BCFZY) compositions [12]. However, proton kinetic studies presently remain limited to the ECR technique.

Proton dynamics have been explored using ab-initio molecular dynamics (MD) simulations [19] and quasi-elastic neutron scattering (QENS) [20–22], nuclear magnetic resonance (NMR) [23], and infrared spectroscopy (IR) [24,25], mainly in pure proton-conducting oxides such as B-site acceptor doped barium zirconates and calcium zirconates. Within TCOs, proton dynamic studies have been relatively scarce. Plekhanov et al. used MD simulations to examine proton location and proton trapping effects in $A^{3+}B^{3+}O_3$ perovskite TCOs [26]. However, this study may be of limited applicability to $A^{2+}B^{4+}O_3$ perovskites like BCFZY4411 because of varying proton – oxygen atom distances depending on the dopant site (A- vs. B-site). To date, the only investigation of compositions closely related to BCFZY4411 is by Chesnokov et al., who utilized density functional theory (DFT) to study B-site doped barium ferrite TCOs [27]. DFT calculations are generally performed under the assumption of 0 K, which does not fully capture the thermally activated nature of proton dynamics. This underscores the importance of the experimental approaches such to validate the reliability of DFT.

The potential applications of BCFZY4411 have been extended, including chemical sensors [28], heterogeneous catalysis [2], and hydrogen permeation membranes [29,30], where the role of protons is of critical importance. Additionally, the presence of five cations across the A- and B-sites of BCFZY4411 allows for great compositional flexibility to enhance ORR and OER [12,15,31,32]. Consequently, a comprehensive understanding of proton behavior in BCFZY4411 is essential for maximizing its performance in various applications and exploring other promising TCOs, beyond the optimization of BCFZY compositions.

This study investigates a wider spectrum of proton behaviors in BCFZY4411, beyond kinetics to encompass thermodynamics (oxygen non-stoichiometry and proton uptake), proton local structure, and dynamics. These aspects are examined primarily through three characterization techniques: 1) thermogravimetric analysis (TGA) for thermodynamics, 2) ^1H solid-state nuclear magnetic resonance (NMR) for local structure and dynamics, and 3) isotope exchange and time-of-flight secondary ion mass spectrometry (ToF-SIMS) for kinetic studies. Furthermore, neutron diffraction (ND) and X-ray absorption near edge structure (XANES) are employed to gather atomic occupancy and oxidation states of B-site cations in BCFZY4411, respectively. These two highly sensitive techniques complement the TGA results by providing critical chemical information that offers insights into the oxygen occupancy in the lattice sites.

2. Experimental methods

2.1. BCFZY4411 synthesis

BCFZY4411 was synthesized by a modified Pechini method, and the details of synthesis are described in the supplementary information (SI). BCFZY4411 powder was pressed into 2 mm thick pellets using a 3/4″ diameter die with 5 wt% polyvinyl alcohol in DI water as a binder. Finally, the pellets were sintered at 1250 °C for 10 h under air and cooled to room temperature (RT) at 1 °C/min, achieving 95–96 % theoretical density. Phase purity was confirmed using X-ray diffraction after both calcination and sintering.

2.2. Neutron diffraction (ND)

ND and structure refinement were performed under ambient conditions on a sample reflecting a selected arbitrary reference state, specifically, 250 °C under dry air. A sintered BCFZY4411 pellet was ground using a SpexMill high-energy ball mill. Following a high temperature dehydration step (500 °C, 2 h, flowing dry air), the sample was equilibrated at 250 °C (3 days, flowing dry air). It was then quenched to RT (directly removed the sample from the heating zone). 2 g of the so-prepared sample was loaded into a 6 mm diameter vanadium can and sealed with a copper seal for ND measurements. ND data were collected at RT to preserve the quenched atomic occupancies, using the high-resolution POWGEN powder diffractometer, using the 1.5 Å frame, at the Spallation Neutron Source (SNS) [33]. The data analysis is described in the SI.

2.3. X-ray absorption near edge structure (XANES)

Transmission mode XANES measurements were conducted under ambient conditions using ground powders of sintered BCFZY4411 pellet (1250 °C, 10 h, air and cooled to room temperature at 1 °C/min). Under air and this slow cooling rate, the sample becomes oxidized relative to the sintering condition (1250 °C). A previous thermal expansion study [12] suggests that the oxidation state fixation in BCFZY4411 occurs between 200 and 400 °C. Duffy et al. also observed indications of oxidation state changes in BCFZY4411 around 300 °C from TGA measurement, narrowing the likely fixation window to 200–300 °C BCFZY441 [34]. The sample preparation is detailed in the SI. Data were collected on the BioXAS beamline at the Canadian Light Source (CLS) synchrotron facility. XANES data were recorded in transmission mode using high energy X-rays from a wiggler insertion device, where the beam was further conditioned by a toroidal mirror collimator, Si (220) double crystal monochromator, focusing mirror, and a set of vertical and horizontal slits. Before each elemental absorption edge measurement, the photon energy of the incident beam was calibrated by performing a XANES measurement of the corresponding standard metal foil. Each XANES measurement was repeated three times to check for reproducibility and then summed for improved statistics. A standard normalization process was applied to each XANES spectra using the ATHENA program [35].

2.4. Thermogravimetric analysis (TGA)

A large dense pellet (15 mm diameter and 2.1 mm thick) was wrapped in a Pt wire and then suspended in a Setaram Setsys evo TGA modified for use under humidified gas environments. While use of a dense pellet significantly increases equilibration times, this approach minimizes surface area, reducing the impact of surface-adsorbed water. The large mass also ensures a high signal-to-noise ratio in the experiments, allowing for the detection of small proton uptake mass signals during hydration.

Mass loss corresponding to oxygen non-stoichiometry (δ) was recorded under both dry and humidified conditions, using a single

sample for the entire series of measurements. The dry state ($p_{H_2O} \approx 0.1$ mbar) was measured under a N_2/O_2 mix to achieve sea-level oxygen partial pressure (p_{O_2} = 209 mbar). p_{O_2} was monitored at the TGA exhaust using a zirconia oxygen sensor (Econox type C-700/C3M). Hydration was achieved by passing part of the N_2 through a Nafion membrane, suspended in an enclosed chamber half-filled with water heated to 66 °C. The dew points (25.0 and 37.2 °C, corresponding to $p_{H_2O} = 31.8$ and 63.6 mbar, respectively) were monitored by a hygrometer (Rotronic HC2) at the TGA exhaust. To avoid oxygen dilution, the N_2 flow rate was decreased by an amount equivalent to the steam added, keeping the total flow rate (and p_{O_2}) constant between dry and humidified experiments. The external oxygen sensor was used to monitor this adjustment. Further measurement and analysis details are explained in the SI.

2.5. ^1H solid-state nuclear magnetic resonance (NMR)

^1H solid-state magic-angle-spinning (MAS, 60 Hz) NMR experiments were performed on a Bruker Avance III-600 spectrometer with a magnetic field of 14.1 T. In addition to recording ^1H resonance positions, local proton dynamics were assessed by performing ^1H T_1 relaxation time measurements using the saturation recovery approach under fast MAS. For comparative purposes, measurements were also made on the well-known proton conductor, $BaZr_{0.8}Y_{0.2}O_{3-\delta}$ (BZY82), using identical NMR data acquisition parameters. Samples consisted of powders of the oxides prepared from a sintered pellets (BCFZY4411: 1250 °C, 10 h, air and cooled to room temperature at 1 °C/min). To achieve hydration, the samples were heat-treated for 4 days at 400 °C under 3 % H_2O. Proton concentrations in BCFZY4411 were quantified ex situ following sequential dehydration treatments (from the maximally hydrated state) at temperatures between 150 and 650 °C at 100 °C steps. Adamantane was used as an internal intensity reference. Full details of the NMR data acquisition steps, including BZY82 synthesis, are provided in the SI.

2.6. H_2O/D_2O isotope exchange and time-of-flight secondary ion mass spectrometry (ToF-SIMS)

Isotope exchange measurements, used to obtain both the H/D surface reaction rate and the bulk H/D diffusivity, were performed on sintered BCFZY4411 pellets of which one side was diamond-polished, achieving a final polish of 0.05 μm. The H_2O/D_2O isotope exchange flow chart is shown in Fig. S9 with details. Post-exchange sample preparation is illustrated in Fig. S10. Before ToF-SIMS measurements, the samples were placed in the ION-TOF (TOF.SIMS 5, Germany) loading chamber overnight to remove the surface water. The sample surface was sputter-cleaned prior to the actual measurement using an Ar^{1200+} cluster ion source (10 keV). Line-scan used a 30 keV Bi^+ primary ion beam of 2 pA total current in static mode, allowing for the acquisition of profiles for $^{16}OH^-$ (m/z = 17.0111) and $^{16}OD^-$ (m/z = 18.0089). The sputter-cleaned area was 700 × 700 μm^2, and 500 × 500 μm^2 of the area was analyzed. Charge compensation was achieved with an electron flood gun, and the extended dynamic range analyzer feature addressed $^{16}OH^-$ saturation. Detected secondary ions containing deuterons in the samples were D^- (m/z = 2.014) and $^{16}OD^-$.

3. Results and discussion

3.1. ND refinement and atomic occupancies

Rietveld refinements, in Fig. 1, show that the BCFZY4411 powder is single phase and well-modeled by the $Pm\bar{3}m$ structure. Short-range antiferromagnetic correlations are evident as diffuse humps at 4.73 and 2.47 Å, but were not included in the model due to their very weak contribution to the refinement. There is some misfit due to the high absorption of Co, which is most severe in the (100) peak at 4.1 Å. The refined lattice parameter, site occupancies, and atomic displacement parameters are shown in Table 1. The unit cell is contracted, compared to previous work. In that prior work, the powder was annealed at 750 °C, resulting in a lower oxygen content; as expected, this powder, annealed at 250 °C, has higher oxidation [36]. Accordingly, the total oxygen occupancy is 0.823, resulting in $\delta = 0.531$. Overall, atomic displacement parameters (ADPs) are higher than typical, especially for the B-site cations. This is likely due to the complexity of four species sharing the octahedral position.

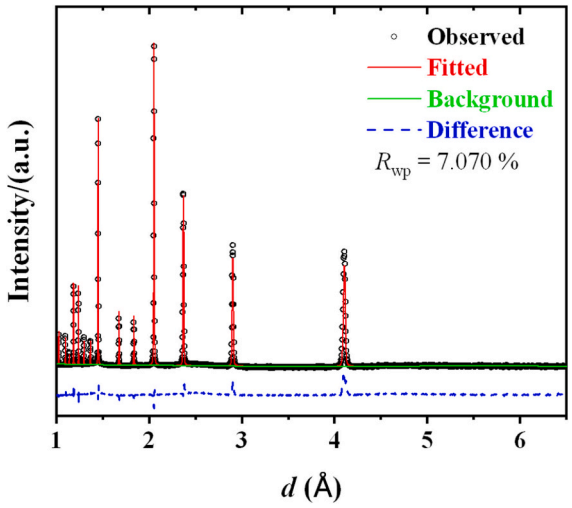

Fig. 1. Observed and modeled neutron powder diffraction data of BCFZY4411 following a quench from 250 °C under dry air. The calculated profile includes the total fit (red line) and the background (green line). (For interpretation of the references to colour in this figure legend, the reader is referred to the web version of this article.)

3.2. Oxidation states of B-site cations

The XANES spectra for the Co and Fe K-edges are displayed in Fig. 2. The K absorption edge energy is assigned to the electronic transition from the 1 s orbital of the atom probed to an unoccupied p level [37]. As the transition metal becomes more oxidized, the absorption edge shifts towards higher energies (i.e., the binding energy for core electrons increases as the screening effect by outer electrons decreases). Comparing the absorption edge energies (defined as $E = E_0$ where normalized μ(E) is 50 % of the edge step) for the measured sample and reference compounds, we determine that the oxidation states for Fe, Zr, and Y in BCFZY4411 are Fe^{3+}, Zr^{4+}, and Y^{3+} (see Fig. S1 for the Zr and Y K-edge XANES spectra). Since none of our reference compounds had a K-edge closely aligned with Co in BCFZY4411, we performed a linear extrapolation of the E_0 values for the reference compounds to estimate the oxidation state to be $Co^{2.9+}$ in BCFZY4411. This approach is justified on the basis of previous works supporting the linear extrapolation (or

Table 1
Refined crystallographic parameters of Space group $Pm\bar{3}m$ was used for Rietveld refinements. R_{wp} and Uiso are weighted profile residual and isotropic atomic displacement parameters (ADPs), respectively.

Lattice parameter						
$a = b = c$ (Å)	4.10256(5)					
V (Å^3)	65.05					
R_{wp}	7.070					
Site occupancy at 250 °C under dry air						
Atom	Ba	O	Co	Fe	Zr	Y
Target site occupancy	1	1	0.4	0.4	0.1	0.1
Refined	1.000(5)	0.823(5)	–	–	–	–
Uiso (Å^2)	Ba	O		Co/Fe/Zr/Y		
	0.0178(4)	0.0234(3)		0.0217(3)		

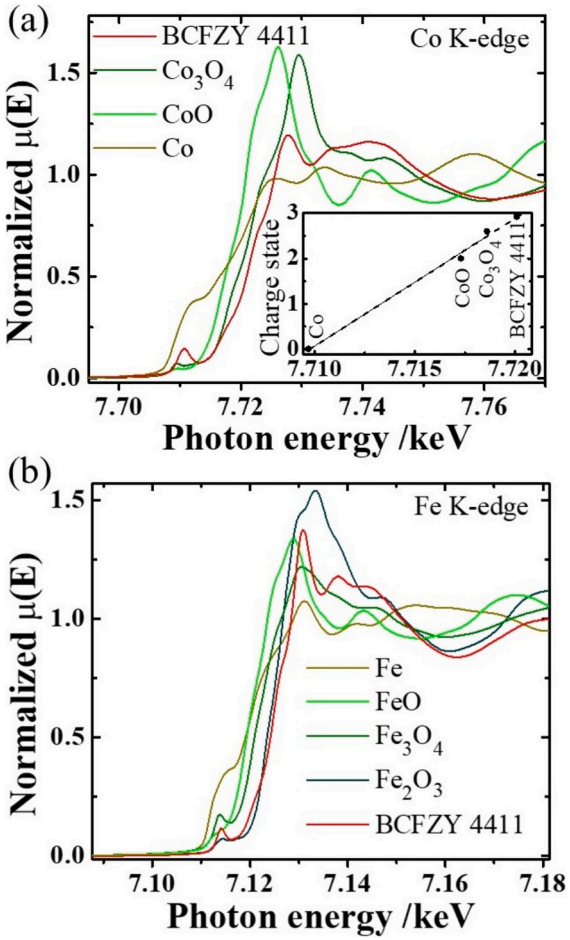

Fig. 2. Normalized XANES spectra of BCFZY4411 along with those of reference compounds for the (a) Co and (b) Fe K-edges measured in transmission mode under ambient conditions. The inset in (a) shows absorption edge energies for different charge states of Co.

interpolation) of the K-edge absorption energies for different reference compounds to estimate the Co oxidation state [38–40]. A similar $Co^{2+/3+}$ mixed valency was reported earlier for BCFZY4411 [41]. The Co valence of 2.9+, along with the fixed valences of the other cations, implies $\delta = 0.47$.

3.3. Equilibrium oxygen non-stoichiometry and proton uptake

TGA experiments and a simple defect model were used to explore the thermal reduction thermodynamics in BCFZY4411. Details of the reduction defect model and the fitting methodology can be found in the SI. The resulting fits, as shown in Fig. 3, provide starting oxygen non-stoichiometry estimates of $\delta = 0.45$ and 0.48 at 50 and 250 °C, respectively, under 209 mbar O_2. The latter agrees well with the non-stoichiometry derived from XANES ($\delta = 0.47$) under the assumption that the oxidation state of BCFZY4411 for the spectroscopy measurement was fixed near 250 °C, and provides further evidence that Fe is redox inactive across these conditions. There is some discrepancy between these values and the ND refinement ($\delta = 0.531$ at 250 °C). This may be due to the presence of cation vacancies, which would be compensated by an increase in δ without affecting the average Co valence. To assess this possibility, the defect model was modified to explore two possible cases: i) A-site cation vacancies, and ii) B-site cation vacancies, for simplicity, in a single species (Fe in this case). These new models were fit to the original TGA mass loss data while constraining the δ to be close to the ND results and using the same ND sample preparation

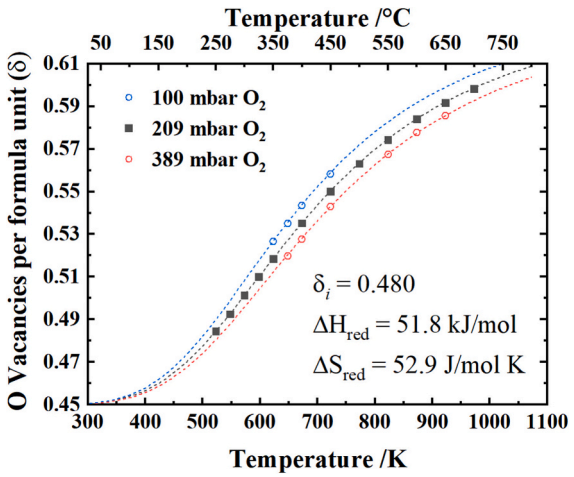

Fig. 3. Oxygen non-stoichiometry (δ) of BCFZY4411 as determined by thermogravimetric analysis under various p_{O_2} levels (as indicated) with the resulting reduction thermodynamic fit curves. Open symbols were not used for fitting.

conditions for modeling. As shown in Fig. 4, although either a 6.3 % loss of Fe (equivalent to a 2.5 % loss of total B-site cations) or a 5.1 % Ba deficiency can explain the differences in δ between the TG and ND results, the reduction thermodynamics are largely unchanged, thus providing confidence in these values.

In general, the results indicate that thermal reduction occurs at

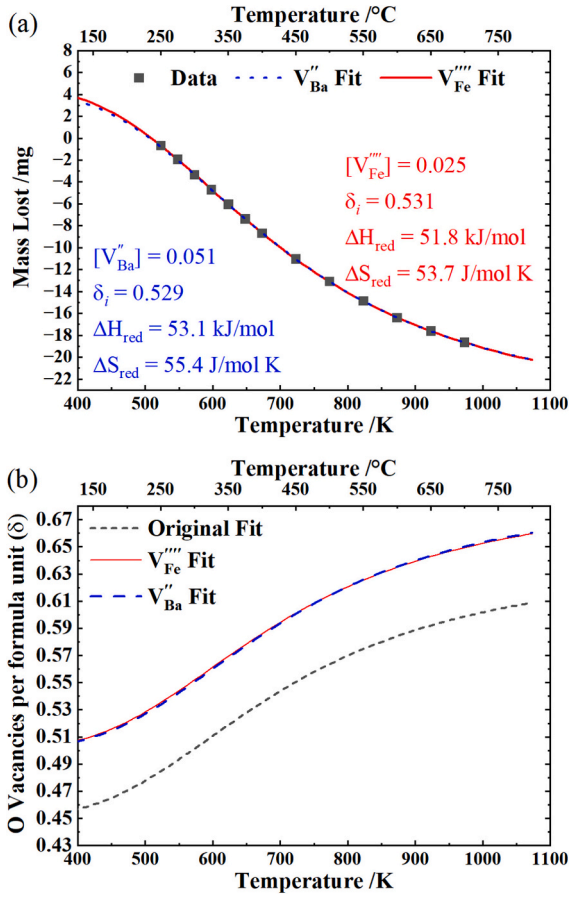

Fig. 4. A comparison of the original fitting results with the addition of cation vacancies for (a) the mass loss experimental results and (b) the resulting oxygen non-stoichiometry with temperature (δ vs T).

temperatures as low as 250 °C and that the δ is significant at all temperatures due to the high level of 3+ cation substitutions on the B-site. The low enthalpy of reduction obtained from the model fit (ΔH_{red} = 51.8 kJ/mol) is not unexpected for positrode materials such as BCFZY4411, which are known to be highly non-stoichiometric [42,43].

A more detailed model that included Co disproportionation was also investigated, as discussed in the SI. While it is possible that Co^{3+} may disproportionate into Co^{2+} and Co^{4+}, the model that included this reaction very slightly worsened the fit, despite the addition of more parameters. Moreover, the derived thermodynamic parameters for the reduction reaction were only marginally impacted, as shown in Table S1. An understanding of the electronic defect changes could help clarify the role of disproportionation; however, it is not possible to gain insight into the electron-hole reaction or electronic defect concentrations using TGA under dry atmospheres, since there is no way to differentiate if δ changes are compensated by localized cation valence changes or more mobile electronic defects. Other work has established very small populations of electron-holes in BCFZY4411 [3], effectively at site fractions on the order of 10^{-5}, consistent with the relatively low electronic conductivity of this material ($\sigma_e \sim 1$ S/cm). A systematic and detailed analysis using Hall-effect measurements would be necessary to examine the influence of temperature and p_{O_2} on the electronic defect populations. Regardless, their small concentrations suggest that even if oxygen and oxygen vacancy reactions participate in electron-hole formation, the reaction does not affect the overall reduction thermodynamics.

For similar reasons, we chose to treat the reduction and hydration processes independently. Preliminary measurements did not show an appreciable change in hydration levels under small changes in p_{O_2} (Fig. S3). Furthermore, as will be demonstrated later, the number of oxygen vacancies filled during hydration does not change the overall oxygen vacancy population enough for there to be competition between the two reactions.

Protons are generated primarily through hydration and/or hydrogenation (Eqs. 1 and 2). Hydration involves the filling of oxygen vacancies with steam (acid-base reaction), producing two protonic defects in the lattice for each molecule of water taken up by the material. In contrast, hydrogenation does not require oxygen vacancies to generate protons but instead consumes electron-holes, leading to proton uptake and gas-phase oxygen (redox reaction).

$$V_O^{\bullet\bullet} + O_O^{\times} + H_2O_{(g)} \rightarrow 2OH_O^{\bullet} \quad (1)$$

$$H_2O_{(g)} + 2O_O^{\times} + 2h^{\bullet} \rightarrow 2OH_O^{\bullet} + \frac{1}{2}O_{2(g)} \quad (2)$$

We performed isotope-labeled TGA experiments, where the mass uptake was observed upon exposure to the same concentration of water vs. deuterated water, as detailed in the SI, to establish that proton incorporation into the BCFZY4411 lattice principally occurs through the uptake of water (hydration), rather than hole-water interactions (hydrogenation). Further TGA measurements were then employed to determine uptake as a function of p_{H_2O} and temperature. The data and resulting fits are shown in Fig. 5.

The bulk proton uptake is modest (e.g., ≈ 0.002 per formula unit at 500 °C under 3 % wet air) as compared to the much higher values (e.g., ≈ 0.13 per formula unit at 500 °C under 2.3 % wet air) seen in electrolytes like BZY82 [44,45]. It is worth noting that the oxygen vacancy concentration obtained under the same p_{O_2} (209 mbar O_2, Fig. 3) is about 100 times higher than the proton concentration obtained across the entire p_{H_2O} range. Using very large pellets allowed us to establish that as much as 1/3 to 1/4 of the low-temperature proton content persists even at high temperatures ($T > 700$ °C), which was unexpected.

Our TGA results deviate from a previously reported proton uptake study in BCFZY4411 [46], which observed proton concentrations as high as 0.022 per formula unit (i.e., approximately one order of magnitude larger than the results reported here). However, that study

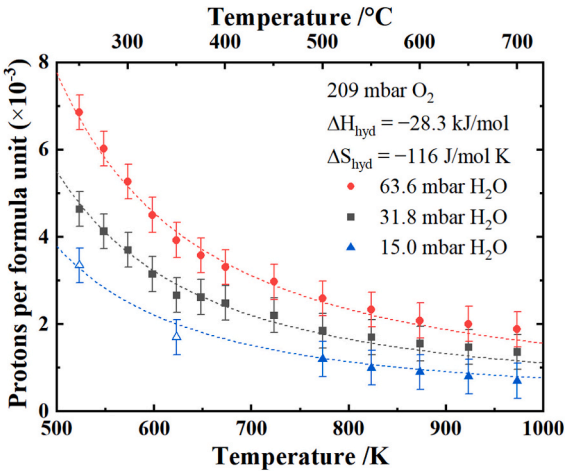

Fig. 5. Hydration results for BCFZY4411 under various p_{H_2O} levels with the resulting thermodynamic fit curves. Open symbols were not used for the fit.

investigated maximum uptake using samples that were thermally reduced and hydrated under 100 ppm O_2 to minimize the electron-hole population. This discrepancy points to the possible general invalidity of the assumption of independence between the hydration and redox reactions. However, the one order of magnitude higher proton concentration reported in this prior work was obtained under test conditions corresponding to approximately four orders of magnitude lower p_{O_2}, so the hydration/redox reaction independence assumption may reasonably hold for the much smaller factor of two changes in p_{O_2} explored in this study. Potential interaction between the hydration and hydrogenation reactions could be pursued via systematic studies under lower oxygen conditions. This is, however, beyond the scope of the present study.

3.4. Proton local structure and dynamics

The ^{1}H NMR spectra, Fig. 6, revealed the presence of both bulk and surface proton species in BCFZY4411. For aid in visualization of the spectral features, the spectra which exclude adamantane, the resonances of which overlap with the surface resonances of the sample, are presented; the signal intensity is scaled according to experimental NMR parameters and total mass to provide approximate quantification. The chemical nature of the species associated with specific resonances was determined by comparison to the spectra of BZY82, also included in Fig. 6. BZY82 exhibit significantly higher proton content compared to BCFZY4411, with higher intensities of the resonances. The most intense peak in BZY82 at ~5.6 ppm is assigned to bulk protons. Its position agrees with previous studies of BZY82 [23] and its intensity is largely retained after mild dehydration at 150 °C. The lower-shift resonances in BZY82, which are significantly diminished after the dehydration, are assigned to surface species based on dedicated literature NMR studies of oxide surfaces [47–49]. In particular, the resonance observed at ~4.0 ppm is assigned to surface-adsorbed water, denoted "surface H_2O", whereas the resonance at 1.3 ppm is assigned to covalently bonded OH-species at the surface. Loss of intensity from these species upon mild dehydration is consistent with their assignment as surface groups. In the case of BCFZY4411, resonances are evident at similar, though not identical, positions. Significantly, in addition to being much lower in overall intensity, the relative intensities of the surface and bulk resonances are inverted such that the bulk signal is extremely low, reflecting the low extent of bulk hydration detected by TGA (Fig. 5).

In comparison to BZY82, the bulk proton resonance in BCFZY4411 displays a downfield shift (appearing at 7.2 ppm as opposed to 5.8 ppm, Fig. 6) and significant broadening (> 1 kHz). Both effects can be explained by the proximity of bulk protons in BCFZY4411 to paramagnetic transition metals, Co^{3+} and Fe^{3+} [50]. The presence of

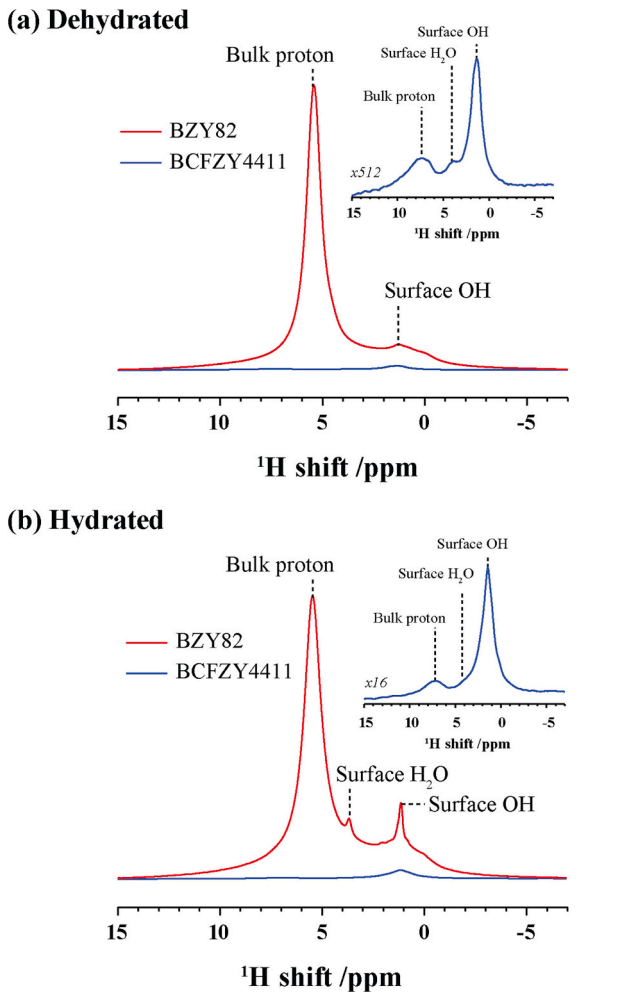

Fig. 6. Proton local structures with peak assignments in BCFZY4411 and BZY82 after (a) mild dehydration under dry air at 150 °C for ~3 h (following maximal hydration) and (b) hydration under 3 % p_{H_2O} at 400 °C for 4 days. Shifts are relative to tetramethyl silane.

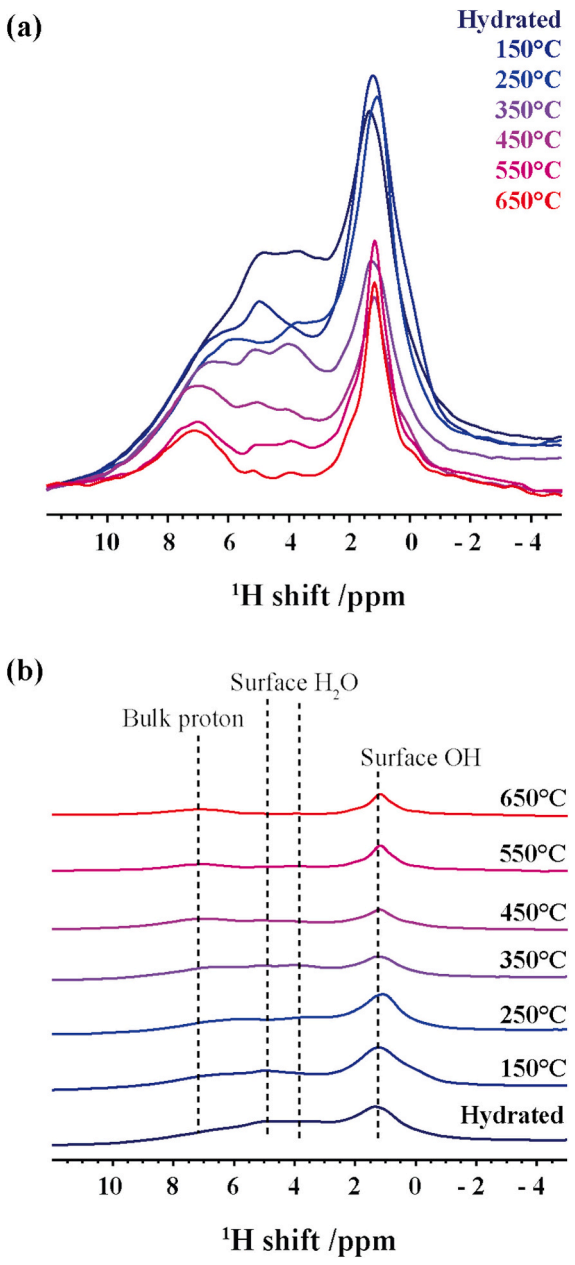

Fig. 7. (a) ^{1}H solid-state MAS NMR of BCFZY4411 dehydrated from 150 to 650 °C at 100 °C intervals. (b) ^{1}H solid-state MAS NMR peak assignments. The slight difference of the hydrated spectrum shown here from that shown in Fig. 6b reflects differences in surface properties, which are highly sample dependent. Shifts are relative to tetramethyl silane.

paramagnetic centers often induces an additional shift (δ_K^p) of the ^{1}H resonance, which is the sum of two terms, δ_K^{pc}, the pseudocontact (dipolar) contribution, and δ_K^c, the Fermi contact contribution. Fermi contact interaction, δ_K^c, is short-range, within 1–3 bonds, and arises due to the delocalization of the unpaired electron spin density onto the nuclear site via through-bond effect [50,51]. When observed, δ_K^c typically results in isotropic paramagnetic shifts that exceed thousands of ppm [52]. In contrast, pseudo-contact interaction, δ_K^{pc}, arises from long-range dipolar coupling between the nuclear magnetic moment and the anisotropic magnetic susceptibility tensor of the paramagnetic centers, leading to relatively small anisotropic paramagnetic shifts. The relatively small downfield shift of the bulk proton in BCFZY4411 indicates that δ_K^{pc} is the dominant contributor with "through-space" dipolar interactions in BCFZY4411.

As shown in Fig. 7, with increasing dehydration temperature from 150 to 650 °C, the integrated NMR intensity of all resonances in BCFZY4411 decreases. The complete set of peak assignments are indicated in Fig. 7b. Notably, the sample represented in Fig. 7 has somewhat different features in the low shift region (3–6 ppm) vs. the sample represented in Fig. 6, in this case revealing two resonances, at 5.0 and 3.8 ppm, for the surface H_2O. The intensities of these resonances furthermore show the greatest decline in response to dehydration treatment. Such behavior provides additional indications that this region reflects the presence of surface H_2O species [53] with variable geometry and broad distribution of hydrogen bonding environments [47,48] and which can be easily removed under mild heating. The resonances at 7.2 and 1.3 ppm (protons in the bulk and surface-OH groups, respectively), in contrast, do not begin to decrease until dehydration is carried out at >350 °C. These resonances are due to chemically bonded species in BCFZY4411. In particular, the remaining surface-OH resonance is relatively sharp, implying well-defined, uniform chemical environments. It is taken to reflect tightly bound-OH groups that reside at internal surfaces, i.e., grain boundaries, in addition to exterior surfaces.

The temperature evolution of the peak intensities is presented in Fig. 8. Here, both the relative integral intensities of all peaks (obtained from the spectra shown in Fig. 7, with deconvolution fitting presented in Table S2 and Fig. S6) and the absolute bulk concentration (obtained using internally referenced spectra, Fig. S7) are displayed. The results

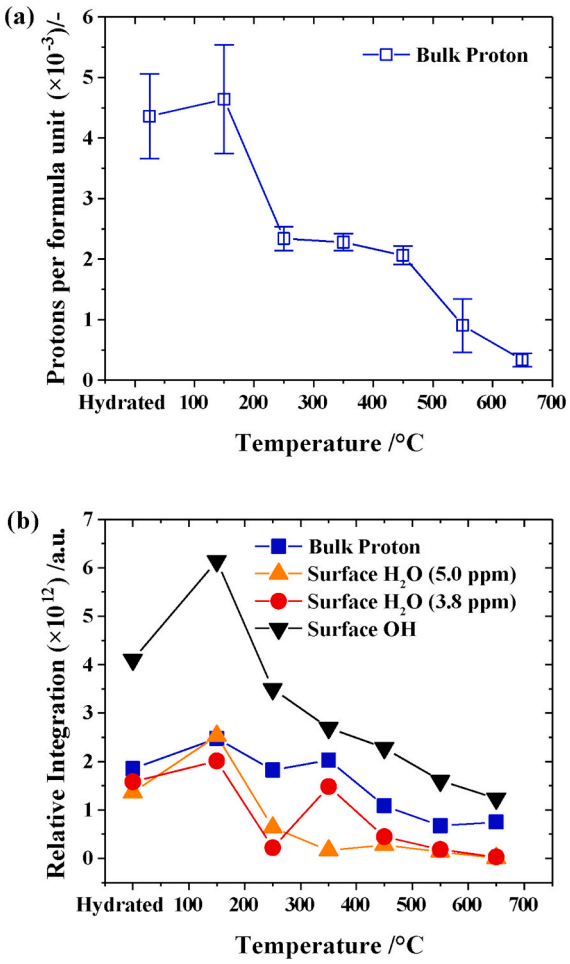

Fig. 8. Examining proton loss in BCFZY4411 using ^{1}H solid-state MAS NMR when dehydrated at 150 to 650 °C under dry air. (a) Bulk proton concentrations are determined via an internal standard, adamantane. (b) Relative NMR resonance areal integrals of separate species in BCFZY4411 to determine hydrogen rate loss for each species.

show an apparent increase in proton content upon dehydration at 100 °C, but this is likely an artifact due the challenges of avoiding rehydration upon removing the sample from the dehydration environment. The absolute proton content in the maximally hydrated state (exposed to 3 % p_{H_2O} at 400 °C for 4 days then quenched) was determined to be 4.4 $\pm$ 0.7 $\times$ 10^{-3} protons per formula unit. This is in reasonable quantitative agreement with the TGA measurements, which indicated 2.49 $\times$ 10^{-3} protons per formula unit for a fully equilibrated sample held at 400 °C under 31.8 mbar p_{H_2O}. For illustrative purposes, the NMR and TGA bulk concentrations are compared in Fig. S8. Due to the non-equilibrium conditions of the dehydration procedure for the former, we refrain from drawing conclusions beyond confirming that the bulk proton concentrations in BCFZY4411 are extremely low, yet detectable, and that the dehydration kinetics are relatively sluggish.

The quantification of the proton concentrations provides further evidence that the resonance at 1.3 ppm is primarily due to -OH groups at grain boundaries. As detailed in the SI, with a particle diameter of ~250 μm, the concentration of surface oxygen atoms is far lower than required to support the number of protons implied by the intensity of the peak at 1.3 ppm. In contrast, the grain size is ~20–50 μm which provides an order of magnitude higher concentration of surface oxygen atoms and sufficient capacity at grain boundaries to achieve the measured OH concentration. The high grain boundary hydration observed in NMR is unlikely to be reflected in the TGA measurements because the former were carried out following maximal hydration and partial, step-wise dehydration treatments without ensuring equilibration, as already noted above.

Turning to the proton dynamics, the T_1 relaxation times for bulk protons in BZY82 and BCFZY4411 are found to be 0.21 and 0.20 s, respectively. The value for surface OH is 3.6 s, whereas the ones for surface H_2O peaks were undetermined due to low resolution. With a spin number of ½ (I = ½), the relaxation process of ^{1}H solid-state NMR is dominated by strong dipole-dipole interactions [54], and the spin-lattice relaxation times are therefore related to the correlation time of ionic motion of protons via the Bloembergen, Purcell, and Pound (BPP) theory. Specifically, the given relationship is as follows [54,55]:

$$\frac{1}{T_1} = C\left[\frac{\tau_c}{1+\omega_L^2\tau_c^2} + \frac{4\tau_c}{(1+4\omega_L^2\tau_c^2)}\right] \quad (3)$$

where C is a constant related to the magnitude of the dipole-dipole interactions, τ_c is the molecular motional correlation time describing the timescale of molecular motions, and ω_L is the Larmor frequency (ω_L ^{1}H = 600.130 MHz). When paramagnetic centers directly couple with the element probed by NMR via Fermi contact interactions, T_1 relaxation times are often on the order of μs ~ ns [46].

The substantially longer T_1 relaxation time measured here implies spatial separation >2 nm between the paramagnetic centers and the ^{1}H atoms and is consistent with the moderate value of the paramagnetic shift via pseudo-contact coupling. With a high concentration of transition metals in BCFZY4411 (80 % of the B-site atoms), the concentration of oxygen sites (at which protons effectively reside) that are >2 nm in distance from paramagnetic elements is small, but large enough to support the measured proton concentration. The similarity of the ^{1}H T_1 relaxation times for BCFZY4411 and BZY82 suggests that the local ^{1}H ion dynamics are similar. This is perhaps unsurprising given the remoteness of the redox active elements from the protons, but also suggests the dynamics are not affected by the differences in proton concentrations. However, as shown below, the macroscopic protonic diffusivity is lower in BCFZY4411 than in BZY82, indicating that Co/Fe can significantly impede long-range proton transport.

3.5. Proton kinetics

The TOF-SIMS tracer exchange measurements yielded the bulk proton tracer diffusivity ($D^*_{H^+}$) and the surface exchange coefficient ($k^*_{H^+}$) at all conditions examined. A representative $^{16}OD^-$ diffusion profile

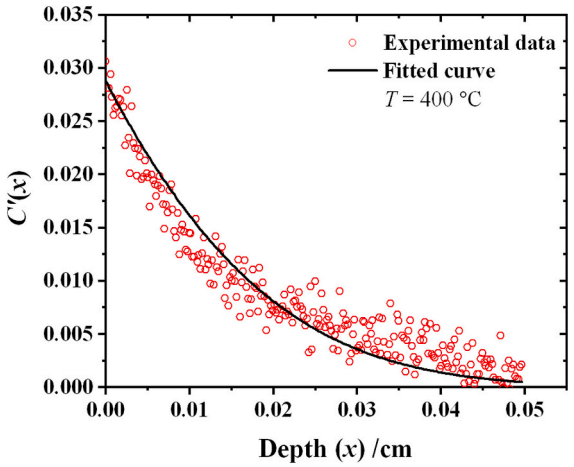

Fig. 9. Normalized $^{16}OD^-$ fraction ($C'(x)$) in BCFZY4411 annealed at 400 °C. Red circles refer to experimental data and black line is the fit to Eq. S26. (For interpretation of the references to colour in this figure legend, the reader is referred to the web version of this article.)

obtained at 400 °C is presented in Fig. 9, along with the corresponding fit used to extract the values of the kinetic properties. In all cases, the shape of the diffusion profile was free of any indication of fast grain-boundary diffusion such as a partially elongated region or/and an extended tail [56]. Thus, while the NMR results suggested a high concentration of grain boundary OH groups (Fig. 8b), such species evidently do not contribute to the macroscopic diffusivity. This is consistent with the slow proton dynamics of these grain boundary surface OH groups, indicated by their significantly larger NMR T_1 relaxation time compared to that of the bulk proton. As shown in Fig. S11, the mass resolution effectively separated $^{16}OD^-$ from $^{18}O^-$ ($m/z = 17.999$) unlike H_2^- ($m/z = 2.015$) and D^-. The intensity ratio of $^{18}O^-$ matched its natural abundance (0.2 %). Data fitting and diffusion parameter extraction using the semi-infinite medium solution are detailed in the SI. For each temperature, measurements were made at multiple spots (at least 6) and the reported $D^*_{H^+}$ and $k^*_{H^+}$ values are averaged across these multiple fits, excluding outliers caused by poor sample conditions (e.g., irregular geometry and surface roughness). All profile fits were achieved with a 95 % confidence interval (max. error of ±5 %). The resulting obtained $D^*_{H^+}$ and $k^*_{H^+}$ values are listed in Table S5.

The $D^*_{H^+}$ and $k^*_{H^+}$ values for BCFZY4411 obtained in this study are compared in Fig. 10 to our previous measurements of the oxygen tracer diffusion properties of BCFZY4411 ($D^*_{O^{2-}}$ and $k^*_{O^{2-}}$) [12]. Notably, the $D^*_{H^+}$ and $k^*_{H^+}$ values are approximately 1.5 to 3 orders of magnitude higher than the corresponding $D^*_{O^{2-}}$ and $k^*_{O^{2-}}$ values, with the difference increasing at lower temperatures. This difference is attributed to the faster migration of protons due to their smaller size and lower mass and is corroborated by similar trends reported in prior studies of proton-conducting oxides and other TCOs [57–60]. The activation energies (E_a) for $D^*_{H^+}$ and $k^*_{H^+}$ were determined to be 31.9 ± 2.8 and 19.2 ± 2.6 kJ/mol, respectively, which are significantly lower than those for $D^*_{O^{2-}}$ and $k^*_{O^{2-}}$ (76 ± 11 and 87.7 ± 2.5 kJ/mol) [12].

Fig. 11 and Table S6 summarize the E_a values for proton tracer and chemical transport properties in various TCOs and proton conductors. Fig. 11 also illustrates E_a values for proton diffusion (hopping and rotation) obtained via bond valence sum (BVS) analysis of BCFZY4411 [67], alongside the E_a extracted from BCFZY4411 electrode polarization resistance (R_p) measured in actual PCFC button-cell tests [6,12,61–66]. The results show good correspondence between the E_a for $D^*_{H^+}$ obtained here with the values obtained by BVS analysis. Notably, the E_a values for

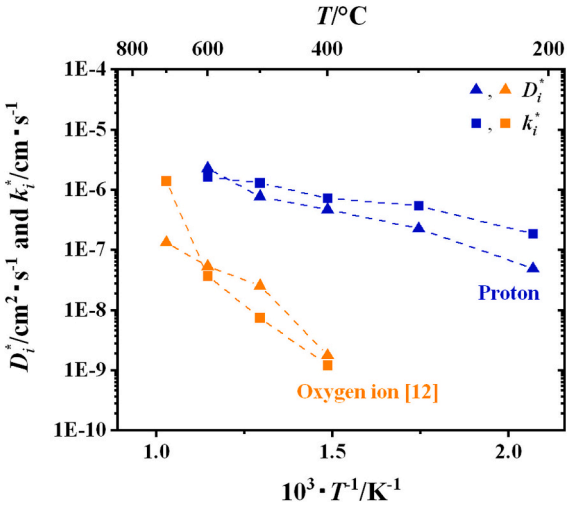

Fig. 10. Arrhenius plot of oxygen [12] and proton tracer diffusion properties of BCFZY4411. *i* represents either a proton (H^+) or an oxygen ion (O^{2-}). The dashed lines are for visual guidance. In all cases, the uncertainty was smaller than the size of the symbols.

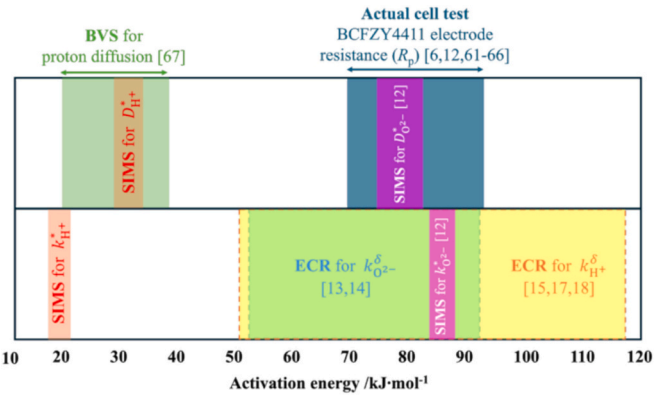

Fig. 11. Comparison of E_a values obtained by BCFZY4411 proton and oxygen-ion kinetic studies through various characterization methods [6,12–15,17,18,61–66] and a theory study [67]. BVS: Bond valance sum analysis, and ECR: Electrical conductivity relaxation.

$D^*_{O^{2-}}$ and $k^*_{O^{2-}}$ in the present work fall within the range observed for the R_p of BCFZY positrodes and complete BCFZY-based PCFC devices. This close correspondence suggests that the oxygen ion kinetics may be rate limiting for ORR/OER, especially at lower temperatures (≤ 500 °C), when using BCFZY4411 and possibly other TCOs as positrodes.

It is also important to note the significant differences in the E_a values of $k^\delta_{H^+}$ obtained from ECR and our $k^\delta_{H^+}$ (see Table S6). This difference is attributed to the higher ECR measurement temperature (500–800 °C) compared to isotope exchange experiments (210–600 °C). Elevated temperatures inhibit the hydration process and may lead to discrepancies in E_a values for $k^\delta_{H^+}$ [68]. Moreover, as discussed below, experimental conditions such as variations in p_{H_2O} during ECR measurement can also influence the chemical potential gradient ($\nabla\mu_i$), thereby affecting $k^\delta_{H^+}$.

While k^* and D^* values reflect the rate at which mobile species overcome kinetic barriers, the macroscopic reaction and transport processes depend additionally on the concentrations of mobile species, that is, on the product terms $X_i k_i^*$ and $X_i D_i^*$, respectively, where X_i represents the fractional (or molar) concentration of species (*i*), and $X_i D_i^*$, through the Nernst-Einstein relation (see SI), is a surrogate for conductivity. In the case of oxygen transport, X_i is the oxygen vacancy concentration, whereas k_i^* and D_i^* refer to the properties of the oxygen ion. In the case of protons, all terms X_i, k_i^*, and D_i^* refer simply to protons, because the proton is an interstitial species. The X_i and conductivity values are provided in Tables S7 and S8 and Fig. S12. In Fig. 12, $X_i k_i^*$ and $X_i D_i^*$ for both protons (this work) and oxygen vacancies (based on our earlier measurements [12]) are presented as functions of temperature. While surface concentrations of carriers may be different than in the bulk, and that is certainly evident for proton concentrations from the ^{1}H NMR studies (Fig. 7), approximating them as equal suffices for the purpose of revealing overall trends.

As shown in Fig. 12, both $X_i k_i^*$ and $X_i D_i^*$ display a cross-over (at T_c) from a low temperature condition in which the proton product terms are greater than the oxygen product terms to a high temperature condition in which the reverse is observed. Formally, this occurs because the product quantities are more temperature-sensitive for oxygen vacancies than protons. Below T_c, $X_{V_O^{\bullet\bullet}} k^*_{O^{2-}}$ and $X_{V_O^{\bullet\bullet}} D^*_{O^{2-}}$ in BCFZY4411 fall below the corresponding proton quantities primarily because of limitations in $k^*_{O^{2-}}$ and $D^*_{O^{2-}}$; the oxygen vacancy concentration remains about 2 orders of magnitude higher than the bulk proton concentration. Conversely, above T_c, $X_{H^+} k^*_{H^+}$ and $X_{H^+} D^*_{H^+}$ fall below the corresponding oxygen quantities because of the low proton concentration. Recognizing that both oxygen ions and protons must be involved in the overall reaction, the occurrence of a cross-over suggests a transition in the ORR/OER

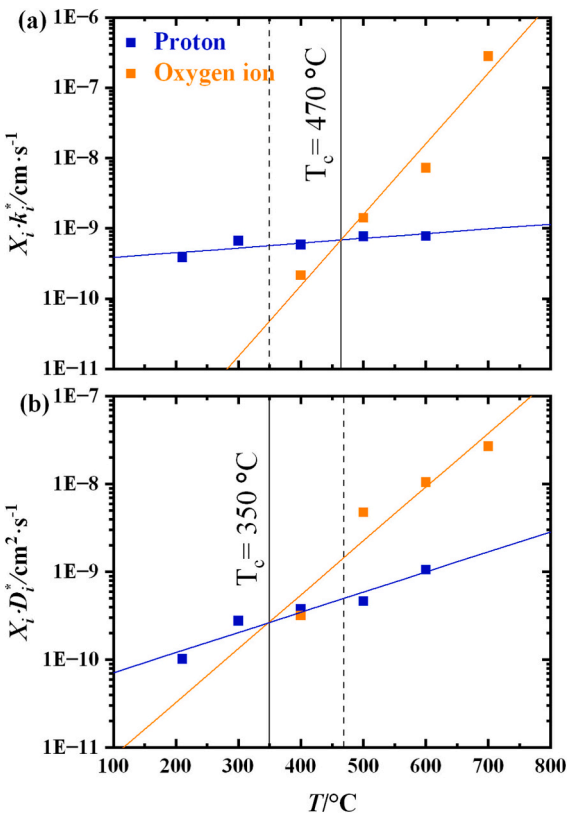

Fig. 12. Temperature dependency of (a) $X_i k_i^*$ and $X_i D_i^*$. Solid lines indicate trendlines, while black solid and dashed vertical lines mark transition temperatures (T_c) and reference T_c values, respectively. The T_c for each plot was determined by the crossover of the trendlines. The ORR/OER are oxygen ion- and proton-limited when $T < T_c$ and $T > T_c$, respectively.

kinetics from oxygen-limited to proton-limited regime as temperature increases. Below T_c, the oxygen properties, specifically, the sluggish oxygen kinetics, limit the process and above T_c, the proton properties, specifically the scarcity of protonic species as a result of dehydration at higher temperatures, limit the process.

From the k_i^* and D_i^* values, it is possible to obtain the critical thickness (L_c) defined as, D_i^*/k_i^*, beyond which bulk diffusion dominates, and below which surface exchange reaction dominates as the rate-limiting step. For both protons and oxygen ions in BCFZY4411, the L_c ranges from several mm to cm. Because the positrode is typically no more than 50 μm in thickness and the particles in positrodes are typically far smaller than this size, we can conclude that the surface reaction step is rate-limiting, and specifically the surface exchange reaction associated with oxygen. Given that L_c provides a practical guideline for optimizing positrode thickness, this observation suggests that the positrode thickness (< 50 μm) has a minimal impact on the positrode performance. Instead, enhancing the oxygen surface exchange reaction becomes more critical for practical applications and increasing positrode thickness could be advantageous for enlarging surface reaction area.

In light of the large L_c, the cross-over in the $X_i k_i^*$ properties is of particular relevance. In this case, the precise value of the transition temperature is unknown due to the uncertainty in the surface X_i values. Indeed, the NMR analysis suggests that surface OH concentrations are greater than in the bulk (Fig. 8b), which may shift the transition to higher than the 470 °C obtained using the bulk concentrations. This could explain the similarity in E_a in R_p values with the E_a values for $k^*_{O^{2-}}$ noted above. Overall, the analysis suggests that increasing $k^*_{O^{2-}}$ may be the critical requirement for enhancing ORR/OER kinetics in BCFZY4411 and other TCOs with high oxygen and proton diffusivity. In the effort to design materials with improved $k^*_{O^{2-}}$, it is essential that the proton kinetics not be sacrificed because high proton diffusivity and surface reaction rates remain essential to the electrochemical processes.

The current results explain why several recent studies enhanced oxygen ion surface exchange kinetics in BCFZY4411 and improved PCFC/PCEC performance. The efforts have been made mainly by modifying the surface of BCFZY4411 using metal oxide nano-catalysts. For instance, Park et al. developed $K_{0.05}Ba_{0.95}Co_{0.4}Fe_{0.4}Zr_{0.1}Y_{0.1}O_{3-\delta}$ (KBCFZY), promoting water-mediated BaO_x exsolution on the surface to increase the active sites for oxygen reactions [41]. This modification significantly improved the oxygen ion chemical surface exchange coefficients compared to non-exsolved BCFZY4411. The enhanced catalytic activity from BaO_x nano-catalyst produced to superior PCFC/PCEC performance compared to using unmodified BCFZY4411 as a positrode, with higher peak power and current densities achieved in PCFC and PCEC modes, respectively. Infiltration techniques have been also employed to modify the BCFZY4411 surface and accelerate the ORR activity, using metal oxide nano-catalyst. Lee et al. infiltrated NiO, known for its high oxygen dissociation and adsorption capabilities, to enhance oxygen surface exchange kinetics on BCFZY4411 and to improve ORR activity in BCFZY4411-$BaCe_{0.7}Zr_{0.1}Y_{0.1}Yb_{0.1}O_{3-\delta}$ composites [65]. They reported that infiltrated nanoparticle NiO not only extended the ORR active sites on BCFZY4411 but also contributed to a lower R_p and higher power density compared to the non-infiltrated positrode composite.

Arrhenius plots of proton tracer and chemical diffusion properties for various proton-conducting oxides and TCOs, including our present work on BCFZY4411, are compared in Fig. 13. Recognizing that the tracer exchange process (H/D) is driven solely by a concentration gradient in the tracer species, whereas chemical exchange in a relaxation experiment involves the combined transport of coupled carriers (such as $V_O^{\bullet\bullet}$ and protonic defects ($OH_O^{\bullet}$) for hydration, as indicated in Eq. 1), the tracer (*) and chemical (δ) terms are related according to equations 5 [56,74] and 6 [75,76] :

$$D_i^* \approx D_i^{\delta}/\gamma_i \tag{5}$$

$$k_i^* \approx k_i^{\delta}/\gamma_i \tag{6}$$

where γ_i is the thermodynamic factor of species, defined as ($\gamma_i = \frac{1}{RT}\frac{\partial \mu_i}{\partial \ln X_i}$). Here, R is the gas constant, T is temperature, and μ_i is the chemical potential of species i.

The thermodynamic factor for protons (γ_{H^+}) can be calculated using knowledge of the proton concentration as a function of conditions, a result given by the TGA measurements (derivation detailed in the SI). In Fig. 13b, three $k^{\delta}_{H^+}$ datasets for BCFZY4411 from ECR studies [15,17,18] are presented. In one case (represented with the ▽ symbols [17] in Fig. 13b), the measurements were performed in a manner suitable for evaluation of γ_{H^+} in that both initial and final states in the relaxation process included finite concentrations of steam. (Dry conditions lead to near-zero initial absolute proton concentrations and hence an undetermined $\partial \ln X_{H^+}$). We employed this dataset to estimate $k^*_{H^+}$ using thermodynamic properties of BCFZY4411 obtained from this work, Table 2. It was assumed that p_{O_2} was controlled to be constant after changing p_{H_2O} during ECR.

The results in Table 2 reveal that ECR measurement conditions lead to γ_{H^+} values around 2. After accounting for this term, the proton diffusivity of BCFZY4411 is within an order of magnitude of the best proton conductors such as $BaCe_{0.9}Y_{0.1}O_{3-\delta}$ (BCY10) [71]. In contrast, $\gamma_{O^{2-}}$ values in transport studies of MIECs are typically 2 orders of magnitude higher (≈100–400) [77,78]. This difference is mainly due to the minimal relative change in the lattice oxygen concentration with the change in p_{O_2}, as reported in previous studies [68,76,77,79–83]. In comparison, X_{H^+} values more than double with the change in p_{H_2O} from 10 to 50 mbar as shown in Table 2. This results in a large value of $\partial \ln X_{H^+}$,

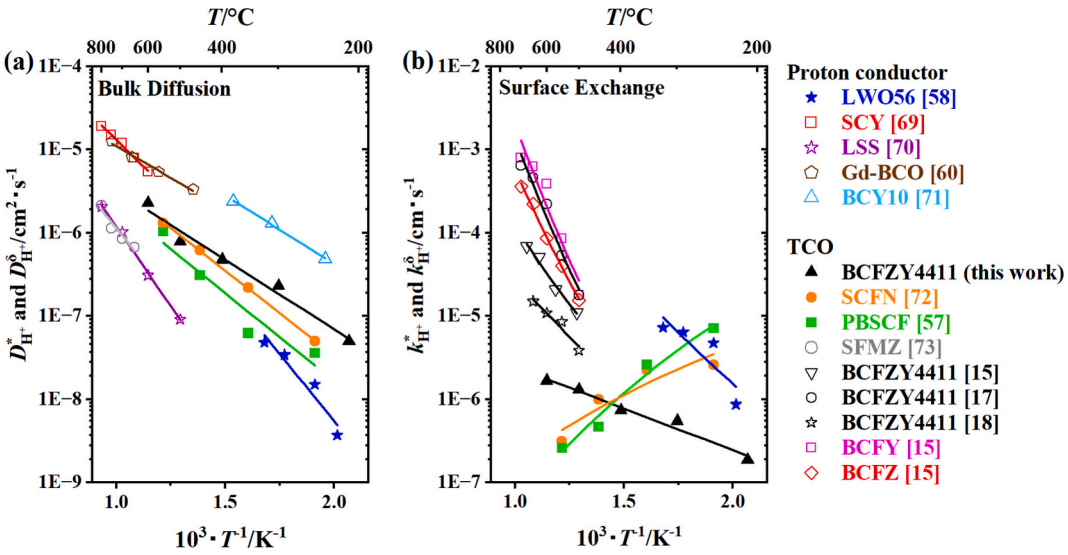

Fig. 13. Arrhenius plots of proton tracer ($X^*_{H^+}$, solid symbol) and chemical ($X^\delta_{H^+}$, open symbol) (a) diffusivities and (b) surface exchange coefficients of various proton conductors and TCOs: $La_{28-x}W_{4+x}O_{54+3x/2v2-3x/2}$ (LWO56, La/W = 5.6) [58], $SrCe_{0.95}Yb_{0.05}O_{3-\delta}$ (SCY) [69], $La_{0.91}Sr_{0.09}ScO_3$ (LSS) [70], $(Ba_{0.965}Gd_{0.035})(Ce_{0.935}Gd_{0.065})O_{2.985}$ (Gd-BCO) [60], $BaCe_{0.9}Y_{0.1}O_{3-\delta}$ (BCY10) [71], BCFZY4411 [15,17,18], $PrBa_{0.5}Sr_{0.5}Co_{1.5}Fe_{0.5}O_{5+\delta}$ (PBSCF) [57], $Sr_{0.9}Ce_{0.1}Fe_{0.8}Ni_{0.2}O_{3-\delta}$ (SCFN) [72], $Sr_2Fe_{1.5}Mo_{0.4}Zr_{0.1}O_{6-\delta}$ (SFMZ) [73], $BaCo_{0.4}Fe_{0.4}Y_{0.2}O_{3-\delta}$ (BCFY) [15], and $BaCo_{0.4}Fe_{0.4}Zr_{0.2}O_{3-\delta}$ (BCFZ) [15]. The solid lines are trendlines.

Table 2
Predicted proton concentration (X_{H^+}) per formula unit for BCFZY4411 from TGA at reported temperatures under p_{O_2} = 209 mbar, with p_{H_2O} varying from 10 to 50 mbar, and the estimated thermodynamic factor (γ_{H^+}) and proton surface exchange coefficient ($k^*_{H^+}$).

T (°C)	500		550		600		650	
p_{H_2O} (mbar)	10	50	10	50	10	50	10	50
X_{H^+} ×10^{-4}	3.32	7.42	2.93	6.55	2.62	5.85	2.37	5.30
γ_{H^+}	2.0027		2.0023		2.0021		2.0018	
Reported $k^\delta_{H^+}$ [17] (cm/s)	3.85E-06		8.5E-06		1.08E-05		1.5E-05	
Inferred $k^*_{H^+}$ $\approx k^\delta_{H^+}/\gamma_{H^+}$ (cm/s)	1.92E-06		4.25E-06		5.39E-06		7.49E-06	
$k^*_{H^+}$ of this work (cm/s)	(1.30 ± 0.10)E-06		–		(1.66 ± 0.05)E-06		–	

which because it appears in the denominator of γ_{H^+}, makes the thermodynamic factor relatively small. The inferred $k^*_{H^+}$ values are therefore smaller than reported values obtained by ECR measurements by a factor of about 2. This constitutes relatively good agreement given the myriad ways in which surfaces can vary. Following Eq. 5, $D^\delta_{H^+}$ values for BCFZY4411 are also estimated to be about twice the $D^*_{H^+}$ values reported here. No literature values of directly measured $D^\delta_{H^+}$ values are available for comparison.

Overall, the behavior of BCFZY4411 relative to other materials, Fig. 13, appears to be embodied in the local dynamics as measured by NMR. BCFZY4411 displays $D^*_{H^+}$ that is higher but $k^*_{H^+}$ that is lower than that of other TCOs (e.g., SCFN and PBSCF). In parallel, the T_1 relaxation time measured for the bulk process in BCFZY4411 is relatively short (0.21 s), whereas the T_1 relaxation time of surface OH is relatively long (3.6 s). While the local dynamics of the other TCOs have not been reported, this large difference in bulk and surface relaxation times is consistent with the behavior BCFZY4411 in comparison to the other materials.

4. Conclusion

Numerous studies have utilized BCFZY4411 as a baseline material to develop modified compositions for promising positrode materials for PCCs and SOCs [3,15,41,62,84,85]. However, most of the fundamental research on BCFZY4411 has focused on oxygen ion kinetics, leaving a gap in understanding proton behavior. This study addresses this gap by investigating the nature of protons in BCFZY4411.

XANES revealed the oxidation states of B-site cations at RT, identifying $Co^{2.9+}$, Fe^{3+}, Zr^{4+}, and Y^{3+}. TGA provided a similar Co oxidation state (2.85), aligning well with XANES results. Additionally, oxygen non-stoichiometry obtained from TGA at 700 °C matched ND data. It was also confirmed that the hydration reaction is the primary mechanism for the proton uptake, and proton uptake was quantified under different p_{H_2O} levels. Both TGA and NMR analyses determined proton uptake to be $\approx 2.0 \times 10^{-3}$ per formula unit at 450 °C under 3 % wet air, significantly lower than that of higher proton-conducting materials like BZY82.

^{1}H solid-state MAS NMR further provided insights into local structure and proton kinetics. Similar T_1 relaxation times between BCFZY4411 and BZY82 indicate comparable local proton motion. Spectral analysis reveals contributions from bulk protons, covalently bonded OH groups, and surface residual water, with changes in concentration at varied dehydration temperatures.

Tracer proton transport properties ($D^*_{H^+}$ and $k^*_{H^+}$) were obtained through the isotope exchange technique and ToF-SIMS measurement. The results demonstrated proton kinetic values 1–3 orders of magnitude higher than those of oxygen ion transport ($D^*_{O^{2-}}$ and $k^*_{O^{2-}}$). The lower E_a for proton transport underscores the need to enhance oxygen ion kinetics to boost ORR and OER activity, especially at lower operating temperatures. The analysis of $X_i k^*_i$ and $X_i D^*_i$ terms revealed oxygen ion- and proton-kinetic dominated regimes. Notably, oxygen surface exchange was identified as a main limiting factor for ORR/OER at targeted

operating temperatures (<500 °C) when BCFZY4411 is utilized in electrochemical applications. Although BCFZY4411 exhibits relatively fast proton kinetics for ORR/OER, its electrochemical performance can be limited by low proton concentration at high temperatures. Thus, increasing proton concentration may also be important for enhancing the performance of BCFZY4411 and further other TCOs as positrode materials.

CRediT authorship contribution statement

Yewon Shin: Writing – original draft, Project administration, Formal analysis, Visualization, Methodology, Writing – review & editing, Resources, Investigation, Validation. **Michael D. Sanders:** Visualization, Writing – original draft, Formal analysis, Validation, Investigation, Writing – review & editing, Methodology. **Erica Truong:** Writing – original draft, Methodology, Investigation, Visualization, Formal analysis, Writing – review & editing, Validation. **Supriyo Majumder:** Visualization, Investigation, Writing – review & editing, Validation, Formal analysis, Writing – original draft, Methodology. **Bernadette Cladek:** Writing – original draft, Methodology, Formal analysis, Writing – review & editing, Investigation, Validation, Visualization. **Michael Walker:** Methodology, Writing – review & editing. **Bright Ogbolu:** Formal analysis. **Rongfu Zhang:** Formal analysis. **Guennadi A. Evmenenko:** Formal analysis. **Yan-Yan Hu:** Supervision, Methodology, Writing – review & editing. **Michael J. Bedzyk:** Writing – review & editing, Methodology, Supervision. **Katharine Page:** Supervision, Writing – review & editing, Methodology. **Sossina M. Haile:** Writing – review & editing, Project administration, Conceptualization, Funding acquisition, Supervision. **Ryan O'Hayre:** Project administration, Funding acquisition, Supervision, Conceptualization, Writing – review & editing.

Declaration of competing interest

The authors declare that they have no known competing financial interests or personal relationships that could have appeared to influence the work reported in this paper.

Data availability

Data will be made available on request.

Acknowledgements

Research primarily supported as part of the Hydrogen in Energy and Information Sciences (HEISs) EFRC, an Energy Frontier Research Center funded by the U.S. Department of Energy (DOE), Office of Science, Basic Energy Sciences (BES), under Award # DE-SC0023450 (data analysis, interpretation). Some of the work was performed in the following core facility, which is a part of Colorado School of Mines (CSM)' Shared Instrumentation Facility (ToF-SIMS RRID: SCR_022049). This work makes use of the TOF-SIMS system at the CSM, which was supported by the National Science Foundation under Grant No. 1726898. All solid-state NMR experiments were performed at the National High Magnetic Field Laboratory. The National High Magnetic Field Laboratory is supported by the National Science Foundation through NSF/DMR-1644779 and the State of Florida. A portion of this research used resources at the SNS, a DOE Office of Science User Facility operated by the Oak Ridge National Laboratory. Authors also thank Roman Chernikov from BioXAS beamline at CLS for the help in XANES measurements. CLS is a national research facility of the University of Saskatchewan, which is supported by the Canada Foundation for Innovation (CFI), the Natural Sciences and Engineering Research Council (NSERC), the National Research Council (NRC), the Canadian Institutes of Health Research (CIHR), the Government of Saskatchewan, and the University of Saskatchewan. We acknowledge Ms. Jayoon Yang at CSM for synthesizing BCFZY4411 used for ^{1}H solid-state MAS NMR.

Appendix A. Supplementary data

Supplementary data to this article can be found online at https://doi.org/10.1016/j.ssi.2025.116962.

References

[1] L.R. Tarutina, M.A. Gordeeva, D.E. Matkin, M.T. Akopian, G.N. Starostin, A. V. Kasyanova, A.P. Tarutin, N.A. Danilov, I.A. Starostina, D.A. Medvedev, Z. Shao, Why do $BaCo_{0.4}Fe_{0.4}Zr_{0.1}Y_{0.1}O_{3-\delta}$-derived complex oxides become one of the most promising electrodes for protonic ceramic electrochemical cells? An explanatory review, Chem. Eng. J. 490 (2024) 151615.

[2] X. Li, L. He, X. Zhong, J. Zhang, S. Luo, W. Yi, L. Zhang, M. Hu, J. Tang, X. Zhou, X. Zhao, B. Xu, Evaluation of A-site Ba^{2+}−deficient $Ba_{1-x}Co_{0.4}Fe_{0.4}Zr_{0.1}Y_{0.1}O_{3-\delta}$ oxides as electrocatalysts for efficient hydrogen evolution reaction, Scanning 1 (2018) 1341608.

[3] C. Xia, Y. Mi, B. Wang, B. Lin, G. Chen, B. Zhu, Shaping triple-conducting semiconductor $BaCo_{0.4}Fe_{0.4}Zr_{0.1}Y_{0.1}O_{3-\delta}$ into an electrolyte for low-temperature solid oxide fuel cells, Nat. Commun. 10 (2019) 1707.

[4] A.A. Samat, M. Darus, N. Osman, N.A. Baharuddin, M. Anwar, AIP Conference Proceedings 2339 (2021) 20233.

[5] M. Papac, V. Stevanović, A. Zakutayev, R. O'Hayre, Triple ionic–electronic conducting oxides for next-generation electrochemical devices, Nat. Mater. 20 (2021) 301–313.

[6] J. Cui, Y. Zhang, Z. Liu, Z. Hu, H.P. Wang, P.Y. Cho, C.Y. Kuo, Y.Y. Chin, C. Te Chen, J. Zhu, J. Zhou, G. Kim, J.Q. Wang, L. Zhang, Key roles of initial calcination temperature in accelerating the performance in proton ceramic fuel cells via regulating 3D microstructure and electronic structure, Small Struct. 5 (2024) 2300439.

[7] C. Herradon, L. Le, C. Meisel, J. Huang, C. Chmura, Y.D. Kim, C. Cadigan, R. O'Hayre, N.P. Sullivan, Proton-conducting ceramics for water electrolysis and hydrogen production at elevated pressure, Front. Energy Res. 10 (2022) 1020960.

[8] C. Duan, R. Kee, H. Zhu, N. Sullivan, L. Zhu, L. Bian, D. Jennings, R. O'Hayre, Highly efficient reversible protonic ceramic electrochemical cells for power generation and fuel production, Nat. Energy 4 (2019) 230–240.

[9] L. Zhu, R. O'Hayre, N.P. Sullivan, High performance tubular protonic ceramic fuel cells via highly-scalable extrusion process, Int. J. Hydrog. Energy 46 (2021) 27784–27792.

[10] H. Qi, Z. Zhao, B. Tu, M. Cheng, Reaction tuned formation of hierarchical $BaCo_{0.4}Fe_{0.4}Zr_{0.1}Y_{0.1}O_{3-\delta}$ cathode, J. Power Sources 455 (2020) 227971.

[11] C. Duan, D. Hook, Y. Chen, J. Tong, R. O'Hayre, Zr and Y co-doped perovskite as a stable, high performance cathode for solid oxide fuel cells operating below 500°C, Energy Environ. Sci. 10 (2017) 176–182.

[12] Y. Shin, Y.D. Kim, M. Sanders, S.P. Harvey, M. Walker, R. O'Hayre, Tuning the co/Fe ratio in $BaCo_xFe_{0.8-x}Zr_{0.1}Y_{0.1}O_{3-\delta}$, a promising triple ionic and electronic conducting oxide, to boost electrolysis and fuel cell performance, J. Mater. Chem. A 10 (2022) 24839–24853.

[13] J.H. Duffy, Y. Meng, H.W. Abernathy, K.S. Brinkman, Surface and bulk oxygen kinetics of $BaCo_{0.4}Fe_{0.4}Zr_{0.2-x}Y_xO_{3-\delta}$ triple conducting electrode materials, Membranes (Basel). 11 (2021) 766.

[14] Y. Meng, J. Duffy, B.T. Na, J. Gao, T. Yang, J. Tong, S. Lee, K.S. Brinkman, Oxygen exchange and bulk diffusivity of $BaCo_{0.4}Fe_{0.4}Zr_{0.1}Y_{0.1}O_{3-\delta}$: quantitative assessment of active cathode material for protonic ceramic fuel cells, Solid State Ionics 368 (2021) 115639.

[15] J.H. Duffy, H.W. Abernathy, K.S. Brinkman, Tuning proton kinetics in $BaCo_{0.4}Fe_{0.4}Zr_{0.2-x}Y_xO_{3-\delta}$ triple ionic-electronic conductors via aliovalent substitution, J. Mater. Chem. A 11 (2023) 8929–8938.

[16] T. Hong, W. Lu, K. Ren, T. Liu, The two-fold diffusion process for proton uptake reaction in BCFZY $e^-/H^+/O^{2-}$ triple conductor measured by electrical conductivity relaxation, Ionics (Kiel). 26 (2020) 5293–5297.

[17] P. Wang, D. Xu, J. Cheng, T. Hong, Proton uptake kinetics and electromotive force in $BaCo_{0.4}Fe_{0.4}Zr_{0.1}Y_{0.1}O_{3-\delta}$ cathode material with $e^-/O^{2-}/H^+$ three mobile carriers for protonic ceramic fuel cells, Ionics (Kiel). 27 (2021) 1185–1192.

[18] Y. Chen, T. Hong, P. Wang, K. Brinkman, J. Tong, J. Cheng, Investigate the proton uptake process of proton/oxygen ion/hole triple conductor $BaCo_{0.4}Fe_{0.4}Zr_{0.1}Y_{0.1}O_{3-\delta}$ by electrical conductivity relaxation, J. Power Sources 440 (2019) 227122.

[19] S. Ray, P.P. Kumar, Investigation of the proton transport mechanism in Sc-doped $CaZrO_3$ using ab-initio molecular dynamics simulations, J. Phys. Chem. C 129 (2025) 9432–9440.

[20] E. Naumovska, J. Orstadius, A. Perrichon, R. Lavén, M.M. Koza, Z. Evenson, M. Karlsson, Localized proton motions in the proton-conducting perovskites $BaZr_{1-x}Sc_xO_3H_x$ (x = 0.10 and 0.50) investigated with Quasielastic Neutron scattering, J. Phys. Chem. C 127 (2023) 24532–24541.

[21] J. Wallis, A. Kruth, F. Demmel, Proton dynamics in a spark-plasma sintered $BaZr_{0.7}Ce_{0.2}Y_{0.1}O_{3-\delta}$ proton conductor investigated by quasi-elastic neutron scattering, Phys. Chem. Chem. Phys. 25 (2023) 13155–13163.

[22] M. Karlsson, Proton dynamics in oxides: insight into the mechanics of proton conduction from quasielastic neutron scattering, Phys. Chem. Chem. Phys. 17 (2015) 26–38.

[23] Y. Yamazaki, F. Blanc, Y. Okuyama, L. Buannic, J.C. Lucio-Vega, C.P. Grey, S. M. Haile, Proton trapping in yttrium-doped barium zirconate, Nat. Mater. 12 (2013) 647–651.

[24] D. Ekanayake, Chalmers University of Technology, 2013.

[25] E. Naumovska, G.K. Nzulu, L. Mazzei, A. Le Febvrier, K. Komander, M. Magnuson, M. Wolff, P. Eklund, M. Karlsson, Local structure of hydrated nanocrystalline films of the proton conductor $BaZr_{1-x}Sc_xO_{3-x/2}$ studied by infrared spectroscopy, Vib. Spectrosc. 130 (2024) 103622.

[26] M.S. Plekhanov, S.L.J. Thomä, M. Zobel, G.J. Cuello, H.E. Fischer, A.A. Raskovalov, A.V. Kuzmin, Correlating proton diffusion in perovskite triple-conducting oxides with local and defect structure, Chem. Mater. 34 (2022) 4785–4794.

[27] A. Chesnokov, D. Gryaznov, E.A. Kotomin, J. Maier, R. Merkle, Protons in (Ga,Sc, In,Y)$^{3+}$–doped $BaFeO_3$ triple conductors — Site energies and migration barriers investigated by density functional theory calculations, Solid State Ionics 421 (2025) 116788.

[28] W. Chen, J. Zou, L. Shan, H. Zhang, W. Wang, J. Jian, T. Yuan, X. Zhang, Y. Zhou, An amperometric high-temperature ammonia sensor based on a $BaCo_{0.4}Fe_{0.4}Zr_{0.1}Y_{0.1}O_{3-\delta}$ triple conductor, Sensors Actuators B Chem. 414 (2024) 135940.

[29] D. Zhang, X. Zhang, X. Zhou, Y. Song, Y. Jiang, B. Lin, Phase stability and hydrogen permeation performance of $BaCo_{0.4}Fe_{0.4}Zr_{0.1}Y_{0.1}O_{3-\delta}$ ceramic membranes, Ceram. Int. 48 (2022) 9946–9954.

[30] C. Zhou, J. Sunarso, J. Dai, R. Ran, Y. Song, F. He, W. Zhou, Z. Shao, Realizing stable high hydrogen permeation flux through $BaCo_{0.4}Fe_{0.4}Zr_{0.1}Y_{0.1}O_{3-\delta}$ membrane using a thin Pd film protection strategy, J. Membr. Sci. 596 (2020) 117709.

[31] R. Ren, Z. Wang, C. Xu, W. Sun, J. Qiao, D.W. Rooney, K. Sun, Tuning the defects of the triple conducting oxide $BaCo_{0.4}Fe_{0.4}Zr_{0.1}Y_{0.1}O_{3-\delta}$ perovskite toward enhanced cathode activity of protonic ceramic fuel cells, J. Mater. Chem. A 7 (2019) 18365–18372.

[32] X. Kuai, G. Yang, Y. Chen, H. Sun, J. Dai, Y. Song, R. Ran, W. Wang, W. Zhou, Z. Shao, Boosting the activity of $BaCo_{0.4}Fe_{0.4}Zr_{0.1}Y_{0.1}O_{3-\delta}$ perovskite for oxygen reduction reactions at low-to-intermediate temperatures through tuning B-site cation deficiency, Adv. Energy Mater. 9 (2019) 1902384.

[33] A. Huq, J.P. Hodges, O. Gourdon, L. Heroux, Powgen: A third-generation highresolution high-throughput powder diffraction instrument at the Spallation Neutron Source, Eur. Powder Diffr. Conf. 1 (2011) 127–136.

[34] J.H. Duffy, N. Birkner, C. Kim, R. Jacobs, D. Morgan, S. Sharma, S.T. Misture, E. M. Kelder, H.W. Abernathy, K.S. Brinkman, Structural and thermodynamic analysis of triple conducting ceramic materials $BaCo_{0.4}Fe_{0.4}Zr_{0.2-X}Y_XO_{3-\delta}$, J. Mater. Chem. A 13 (2025) 10147–10159.

[35] B. Ravel, M. Newville, ATHENA, ARTEMIS, HEPHAESTUS: data analysis for X-ray absorption spectroscopy using IFEFFIT, J. Synchrotron Radiat. 12 (2005) 537–541.

[36] B. Cladek, K. Agyekum, Y. Shin, W. R. Meier, J. Liu, R. O'Hayre, S. M. Haile and K. Page, Subtleties in the structure and magnetic properties of the triple conducting perovskite, BaCo0.4Fe0.4Zr0.1Y0.1O3–δ (accepted), Phys. Rev. Mater.

[37] L. Shan Kau, D.J. Spira-solomon, J.E. Spira-Solomon-Penner-Hahn, K.O. Hodgson, E.I. Solomon, X-ray absorption edge determination of the oxidation state and coordination number of copper: application to the type 3 site in Rhus vernicifera laccase and its reaction with oxygen, J. Am. Chem. Soc. 109 (1987) 6433–6442.

[38] P. Schrapers, S. Mebs, S. Goetzl, S.E. Hennig, H. Dau, H. Dobbek, M. Haumann, Axial ligation and redox changes at the cobalt ion in cobalamin bound to Corrinoid Iron-sulfur protein (CoFeSP) or in solution characterized by XAS and DFT, PLoS One 11 (2016) 1–20.

[39] S. Wang, Q. Jiang, S. Ju, C.S. Hsu, H.M. Chen, D. Zhang, F. Song, Identifying the geometric catalytic active sites of crystalline cobalt oxyhydroxides for oxygen evolution reaction, Nat. Commun. 13 (2022) 6650.

[40] A. Badreldin, J. Abed, N. Hassan, A. El-Ghenymy, W. Suwaileh, Y. Wubulikasimu, Z.K. Ghouri, K. Youssef, D. Kumar, K. Elsaid, E.H. Sargent, A. Abdel-Wahab, Sulfide interlayered cobalt-based oxynitrides for efficient oxygen evolution reaction in neutral pH water and seawater, Appl. Catal. B Environ. 330 (2023) 122599.

[41] K. Park, M. Saqib, H. Lee, D. Shin, M. Jo, K.M. Park, M. Hamayun, S.H. Kim, S. Kim, K.S. Lee, R. O'Hayre, M. Choi, S.J. Song, J.Y. Park, Water-mediated exsolution of nanoparticles in alkali metal-doped perovskite structured triple-conducting oxygen electrocatalysts for reversible cells, Energy Environ. Sci. 17 (2024) 1175–1188.

[42] D. Jeong, A. Jun, Y.W. Ju, J. Hyodo, J. Shin, T. Ishihara, T.H. Lim, G. Kim, Structural, electrical, and electrochemical characteristics of $LnBa_{0.5}Sr_{0.5}Co_{1.5}Fe_{0.5}O_{5+\delta}$ (Ln=Pr, Sm, Gd) as Cathode materials in intermediate-temperature solid oxide fuel cells, Energy Technol. 5 (2017) 1337–1343.

[43] E. Vøllestad, M. Schrade, J. Segalini, R. Strandbakke, T. Norby, Relating defect chemistry and electronic transport in the double perovskite $Ba_{1-x}Gd_{0.8}La_{0.2+x}Co_2O_{6-\delta}$ (BGLC), J. Mater. Chem. A 5 (2017) 15743–15751.

[44] K.D. Kreuer, S. Adams, W. Münch, A. Fuchs, U. Klock, J. Maier, Proton conducting alkaline earth zirconates and titanates for high drain electrochemical applications, Solid State Ionics 145 (2001) 295–306.

[45] Y. Yamazaki, C.K. Yang, S.M. Haile, Unraveling the defect chemistry and proton uptake of yttrium-doped barium zirconate, Scr. Mater. 65 (2011) 102–107.

[46] R. Zohourian, R. Merkle, G. Raimondi, J. Maier, Mixed-conducting perovskites as cathode materials for protonic ceramic fuel cells: understanding the trends in proton uptake, Adv. Funct. Mater. 28 (2018) 1801241.

[47] R. Leboda, V.V. Turov, M. Marciniak, A.A. Malygin, A.A. Malkov, Characteristics of the hydration layer structure in porous titania-silica obtained by the chemical vapor deposition method, Langmuir 15 (1999) 8441–8446.

[48] J. Chen, M.A. Hope, Z. Lin, M. Wang, T. Liu, D.M. Halat, Y. Wen, T. Chen, X. Ke, P. C.M.M. Magusin, W. Ding, X. Xia, X.P. Wu, X.Q. Gong, C.P. Grey, L. Peng, Interactions of oxide surfaces with water revealed with solid-state NMR spectroscopy, J. Am. Chem. Soc. 142 (2020) 11173–11182.

[49] V.M. Gun'ko, V.V. Turov, Structure of hydrogen bonds and 1H NMR spectra of water at the interface of oxides, Langmuir 15 (1999) 6405–6415.

[50] A.J. Pell, G. Pintacuda, C.P. Grey, Paramagnetic NMR in solution and the solid state, Prog. Nucl. Magn. Reson. Spectrosc. 111 (2019) 1–271.

[51] M.A. Islam, M. Autillo, L. Guérin, C. Tamain, P. Moisy, H. Bolvin, C. Berthon, Dipolar and contact paramagnetic NMR chemical shifts in An^{IV} Complexes with Dipicolinic acid derivatives, Inorg. Chem. 61 (2022) 10329–10341.

[52] E. Ravera, Phase distortion-free paramagnetic NMR spectra, J. Magn. Reson. Open 8 (2021) 100022.

[53] H. Cho, P.B. Shepson, L.A. Barrie, J.P. Cowin, R. Zaveri, NMR investigation of the quasi-brine layer in ice/brine mixtures, J. Phys. Chem. B 106 (2002) 11226–11232.

[54] H. Maekawa, N. Kashii, J.I. Kawamura, Y. Hinatsu, T. Yamamura, High Temperature 1H NMR Study of Proton Conducting Oxide $SrCe_{0.95}Y_{0.05}H_{0.004}O_{3-\delta}$, Solid State Ionics 122 (1999) 231–236.

[55] D. Brinkmann, NMR studies of superionic conductors, Prog. Nucl. Magn. Reson. Spectrosc. 24 (1992) 527–552.

[56] R.A. De Souza, J.A. Kilner, J.F. Walker, SIMS study of oxygen tracer diffusion and surface exchange in $La_{0.8}Sr_{0.2}MnO_{3+\delta}$, Mater. Lett. 43 (2000) 43–52.

[57] A. Seong, J. Kim, D. Jeong, S. Sengodan, M. Liu, S. Choi, G. Kim, Electrokinetic proton transport in triple ($H^+/O^{2-}/e^-$) conducting oxides as a key descriptor for highly efficient protonic ceramic fuel cells, Adv. Sci. 8 (2021) 2004099.

[58] R. Hancke, S. Fearn, J.A. Kilner, R. Haugsrud, Determination of proton- and oxide ion tracer diffusion in lanthanum tungstate (La/W = 5.6) by means of ToF-SIMS, Phys. Chem. Chem. Phys. 14 (2012) 13971–13978.

[59] D.-K. Lim, T.-R. Lee, B. Singh, J.-Y. Park, S.-J. Song, Partial conductivities and chemical diffusivities of multi-ion transporting $BaZr_xCe_{0.85-x}Y_{0.15}O_{3-\delta}$ (x = 0, 0.2, 0.4 and 0.6), J. Electrochem. Soc. 161 (2014) F991–F1001.

[60] K.D. Kreuer, E. Schönherr, J. Maier, Proton and oxygen diffusion in $BaCeO_3$ based compounds: A combined thermal gravimetric analysis and conductivity study, Solid State Ionics 70–71 (1994) 278–284.

[61] F. He, M. Liang, W. Wang, R. Ran, G. Yang, W. Zhou, Z. Shao, High-performance proton-conducting fuel cell with B-site-deficient perovskites for all cell components, Energy Fuel 34 (2020) 11464–11471.

[62] M. Liang, Y. Song, D. Liu, L. Xu, M. Xu, G. Yang, W. Wang, W. Zhou, R. Ran, Z. Shao, Magnesium tuned triple conductivity and bifunctionality of $BaCo_{0.4}Fe_{0.4}Zr_{0.1}Y_{0.1}O_{3-\delta}$ perovskite towards reversible protonic ceramic electrochemical cells, Appl. Catal. B Environ. 318 (2022) 121868.

[63] X. Wang, W. Li, C. Zhou, M. Xu, Z. Hu, C.W. Pao, W. Zhou, Z. Shao, Enhanced proton conduction with low oxygen vacancy concentration and favorable hydration for protonic ceramic fuel cells cathode, ACS Appl. Mater. Interfaces 15 (2022) 1339–1347.

[64] R. Song, X. Zhang, D. Huan, X. Li, N. Shi, C. Xia, R. Peng, Y. Lu, A novel triple-conductive cathode with high efficiency and stability for protonic ceramic fuel cells, Int. J. Hydrog. Energy 48 (2023) 32943–32954.

[65] H. Lee, H. Jung, C. Kim, S. Kim, I. Jang, H. Yoon, U. Paik, T. Song, Enhanced electrochemical performance and durability of the $BaCo_{0.4}Fe_{0.4}Zr_{0.1}Y_{0.1}O_{3-\delta}$ Composite cathode of protonic ceramic fuel cells via forming nickel oxide nanoparticles, ACS Appl. Energy Mater. 4 (2021) 11564–11573.

[66] C. Zhou, D. Liu, M. Fei, X. Wang, R. Ran, M. Xu, W. Wang, W. Zhou, R. O'Hayre, Z. Shao, Cathode water management towards improved performance of protonic ceramic fuel cells, J. Power Sources 556 (2023) 232403.

[67] K. Agyekum, Z. Jiang, B. Cladek, Y. Shin, R. O'Hayre, C. Wolverton, J. Liu and K. Page, Compositional Effects on Proton and Oxygen Ionic Transport of $BaCo_xFe_{0.8-x}Zr_{0.1}Y_{0.1}O_{3-d}$ (in preparation).

[68] R. Hancke, R. Haugsrud, The correlation between surface kinetic and bulk diffusion properties of proton conducting oxides, Solid State Ionics 306 (2017) 48–54.

[69] H. Uchida, H. Yoshikawa, T. Esaka, S. Ohtsu, H. Iwahara, Formation of protons in SrCeO3-based proton conducting oxides. Part II. Evaluation of proton concentration and mobility in Yb-doped $SrCeO_3$, Solid State Ionics 36 (1989) 89–95.

[70] A.S. Farlenkov, M.I. Vlasov, N.M. Porotnikova, I.A. Bobrikov, A.V. Khodimchuk, M. V. Ananyev, Hydrogen diffusivity in the Sr-doped $LaScO_3$ proton-conducting oxides, Int. J. Hydrog. Energy 45 (2020) 23455–23468.

[71] K.D. Kreuer, T. Dippel, Y.M. Baikov, J. Maier, Water solubility, proton and oxygen diffusion in acceptor doped $BaCeO_3$: A single crystal analysis, Solid State Ionics 86–88 (1996) 613–620.

[72] Y. Song, J. Liu, Y. Wang, D. Guan, A. Seong, M. Liang, M.J. Robson, X. Xiong, Z. Zhang, G. Kim, Z. Shao, F. Ciucci, Nanocomposites: A new opportunity for developing highly active and durable bifunctional air electrodes for reversible protonic ceramic cells, Adv. Energy Mater. 11 (2021) 2101899.

[73] R. Ren, Z. Wang, X. Meng, X. Wang, C. Xu, J. Qiao, W. Sun, K. Sun, Tailoring the oxygen vacancy to achieve fast intrinsic proton transport in a perovskite cathode for protonic ceramic fuel cells, ACS Appl. Energy Mater. 3 (2020) 4914–4922.

[74] R.A. De Souza, J.A. Kilner, Oxygen transport in $La_{1-x}Sr_xMn_{1-y}Co_yO_{3\pm\delta}$ perovskites part I Oxygen tracer diffusion, Solid State Ionics 106 (1998) 175–187.

[75] J.A. Lane, S.J. Benson, D. Waller, J.A. Kilner, Oxygen transport in $La_{0.6}Sr_{0.4}Co_{0.2}Fe_{0.8}O_{3-\delta}$, Solid State Ionics 121 (1999) 201–208.

[76] A.V. Berenov, A. Atkinson, J.A. Kilner, E. Bucher, W. Sitte, Oxygen tracer diffusion and surface exchange kinetics in $La_{0.6}Sr_{0.4}CoO_{3-\delta}$, Solid State Ionics 181 (2010) 819–826.

[77] F. Mauvy, J.M. Bassat, E. Boehm, P. Dordor, J.C. Grenier, J.P. Loup, Chemical oxygen diffusion coefficient measurement by conductivity relaxation-correlation between tracer diffusion coefficient and chemical diffusion coefficient, J. Eur. Ceram. Soc. 24 (2004) 1265–1269.

[78] M.W. den Otter, University of Enschede, 2000.

[79] J. Maier, Physical Chemistry of Ionic Materials: Ions and Electrons in Solids 1, Wiley, 2004.
[80] V.A. Sadykov, V.S. Muzykantov, N.F. Yeremeev, V.V. Pelipenko, E.M. Sadovskaya, A.S. Bobin, Y.E. Fedorova, D.G. Amanbaeva, A.L. Smirnova, Solid oxide fuel cell cathodes: importance of chemical composition and morphology, Catal. Sustain. Energy 2 (2016) 57–70.
[81] J. Claus, M. Leonhardt, J. Maier, Tracer diffusion and chemical diffusion of oxygen in acceptor doped $SrTiO_3$, J. Phys. Chem. Solids 61 (2000) 1199–1207.
[82] J. Maier, Interaction of oxygen with oxides: how to interpret measured effective rate constants? Solid State Ionics 135 (2000) 575–588.
[83] R. Hancke, Z. Li, R. Haugsrud, Hydrogen surface exchange on proton conducting oxides studied by gas phase analysis with mass spectrometry, J. Membr. Sci. 439 (2013) 68–77.
[84] R. Ren, X. Yu, Z. Wang, C. Xu, T. Song, W. Sun, J. Qiao, K. Sun, Fluorination inductive effect enables rapid bulk proton diffusion in $BaCo_{0.4}Fe_{0.4}Zr_{0.1}Y_{0.1}O_{3-\delta}$ perovskite oxide for high-activity protonic ceramic fuel cell cathode, Appl. Catal. B Environ. 317 (2022) 121759.
[85] M. Liang, Y. Zhu, Y. Song, D. Guan, Z. Luo, G. Yang, S.P. Jiang, W. Zhou, R. Ran, Z. Shao, A new durable surface nanoparticles-modified perovskite cathode for protonic ceramic fuel cells from selective cation Exsolution under oxidizing atmosphere, Adv. Mater. 34 (2022) 2106379.